nature cell biology

Pivoting of microtubules around the spindle pole accelerates kinetochore capture

Iana Kalinina[1,4], Amitabha Nandi[2,4], Petrina Delivani[1], Mariola R. Chacón[1], Anna H. Klemm[1], Damien Ramunno-Johnson[1], Alexander Krull[1], Benjamin Lindner[2,4], Nenad Pavin[1,2,3,5] and Iva M. Tolić-Nørrelykke[1,5]

During cell division, spindle microtubules attach to chromosomes through kinetochores, protein complexes on the chromosome[1]. The central question is how microtubules find kinetochores. According to the pioneering idea termed search-and-capture, numerous microtubules grow from a centrosome in all directions and by chance capture kinetochores[2–4]. The efficiency of search-and-capture can be improved by a bias in microtubule growth towards the kinetochores[5,6], by nucleation of microtubules at the kinetochores[7–9] and at spindle microtubules[10,11], by kinetochore movement[9], or by a combination of these processes[12–14]. Here we show in fission yeast that kinetochores are captured by microtubules pivoting around the spindle pole, instead of growing towards the kinetochores. This pivoting motion of microtubules is random and independent of ATP-driven motor activity. By introducing a theoretical model, we show that the measured random movement of microtubules and kinetochores is sufficient to explain the process of kinetochore capture. Our theory predicts that the speed of capture depends mainly on how fast microtubules pivot, which was confirmed experimentally by speeding up and slowing down microtubule pivoting. Thus, pivoting motion allows microtubules to explore space laterally, as they search for targets such as kinetochores.

At the onset of mitosis in the fission yeast *Schizosaccharomyces pombe*, the three pairs of sister kinetochores and the two spindle pole bodies (SPBs) are clustered together[15]. As the nuclear envelope does not break down during mitosis, microtubules in prometaphase are inside the nucleus[16,17], whereas the SPBs are embedded in the nuclear envelope. When the SPBs start to nucleate microtubules, microtubules growing from one SPB interact with microtubules growing from the other SPB, thereby forming the spindle, which grows and separates the SPBs. At the same time, the kinetochores interact with the microtubules and become integrated into the nascent spindle. If the spindle disassembles during metaphase, it is able to reassemble, including capturing kinetochores that have been lost in the nucleoplasm, that is, located away from the SPBs (ref. 18). To induce lost kinetochores, we disassembled the spindle by exposing the cells in metaphase to cold stress (Fig. 1a). After microtubule disassembly, some kinetochores are lost in the nucleoplasm, whereas the remaining kinetochores are at the SPBs. Once the cold stress is relieved, microtubules regrow from the SPBs, which are separated at this time. Some microtubules growing from one SPB come into contact with microtubules growing from the other SPB, thereby reassembling the central spindle. Other intranuclear microtubules, termed polar microtubules, grow from the SPB at an oblique angle with respect to the spindle (Fig. 1a). Microtubules growing from the kinetochore were not observed ($n = 54$ cells); thus, the mechanism of capture based on microtubule nucleation at the kinetochore[8] is not relevant for fission yeast. Polar microtubules capture lost kinetochores, retrieve them to the SPB, and mitosis progresses regularly.

To quantify the kinetics of kinetochore capture, we measured how the number of lost kinetochores decreased in time, by using the lost kinetochore assay[18,19] and fixing the cells at one minute intervals after the cold stress was relieved (Fig. 1b; the average number of lost kinetochores is divided by that at 0 min). Immediately after relieving the cold stress, there was on average 0.5 lost kinetochores per metaphase cell (Supplementary Fig. S1). Afterwards, the number of lost kinetochores per metaphase cell decreased in time[18]. The average number of lost kinetochores was halved within 3–4 min, which defines the typical capture time in this system (Fig. 1b; Supplementary Fig. S1 shows results of individual experiments).

Live-cell imaging of cells with kinetochores labelled in red (Ndc80–tdTomato) and microtubules in green (α-tubulin–GFP)

[1]Max Planck Institute of Molecular Cell Biology and Genetics, 01307 Dresden, Germany. [2]Max Planck Institute for the Physics of Complex Systems, 01187 Dresden, Germany. [3]Department of Physics, Faculty of Science, University of Zagreb, 10002 Zagreb, Croatia. [4]Present address: European Molecular Biology Laboratory, Meyerhofstrasse 1, 69117 Heidelberg, Germany (I.K.); Department of Molecular, Cellular and Developmental Biology, Yale University, New Haven, Connecticut 06520, USA (A.N.); Bernstein Center for Computational Neuroscience Berlin and Physics Department of Humboldt University Berlin, 10115 Berlin, Germany (B.L.). [5]Correspondence should be addressed to N.P. or I.M.T-N. (e-mail: npavin@phy.hr or tolic@mpi-cbg.de)

Received 8 May 2012; accepted 5 November 2012; published online 9 December 2012; DOI: 10.1038/ncb2640

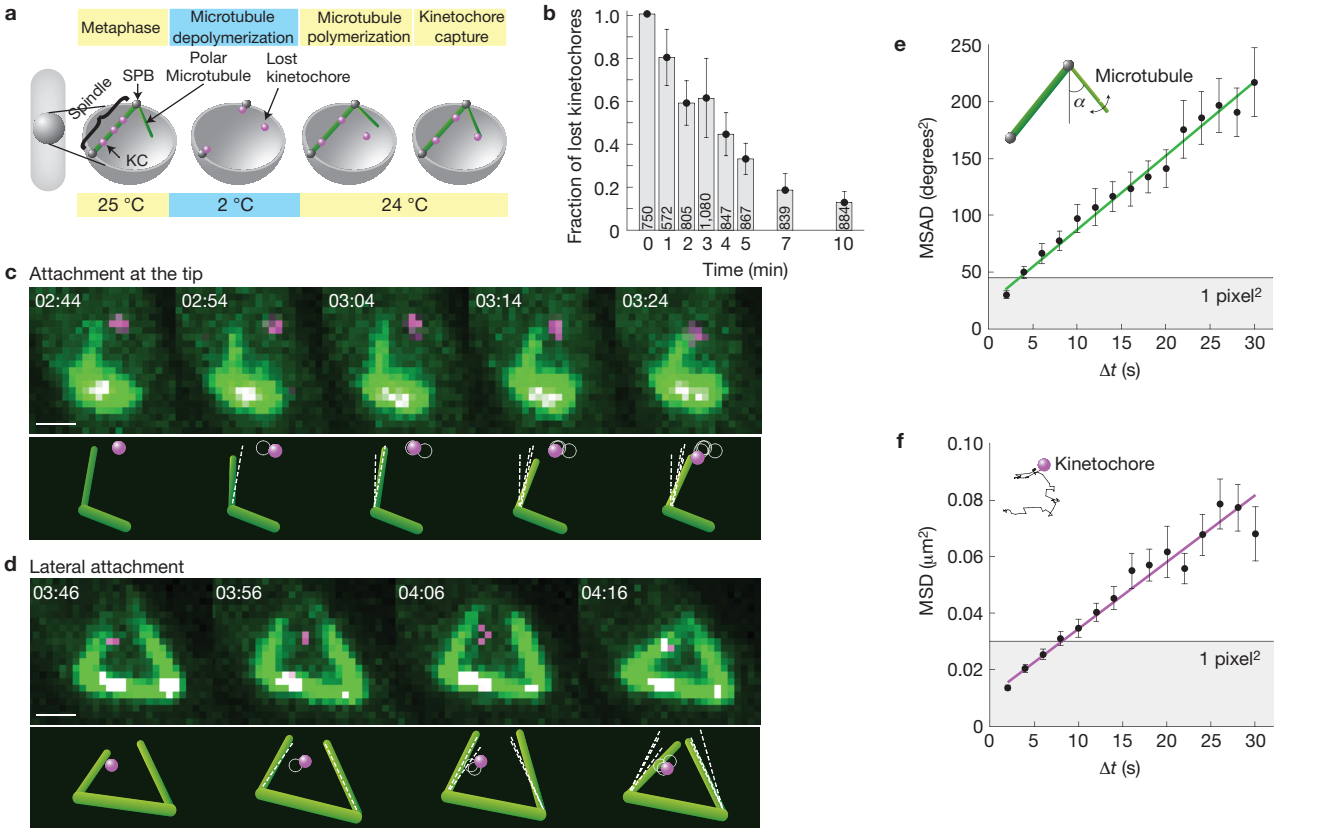

Figure 1 Kinetics of kinetochore capture and the behaviour of microtubules and kinetochores. (**a**) Experimental protocol. Mitotic cells were cooled to 2 °C to depolymerize microtubules (see Methods). Consequently, some kinetochores were lost in the nucleoplasm. After the temperature was increased to 24 °C, microtubules grew from the SPBs and captured lost kinetochores. (**b**) Normalized average fraction of lost kinetochores as a function of time after relieving cold stress (mean ± s.e.m., $n = 13$, see also Supplementary Fig. S1). The numbers inside the bars represent the total number of metaphase cells (strains AH01 and KI061, Supplementary Table S1). (**c**,**d**) Time-lapse images and the corresponding drawings of 2 examples of kinetochore capture, where the kinetochore was captured close to the microtubule tip (**c**) or away from the tip (**d**). The cells (strain AH01) expressed α-tubulin–GFP, shown in green, and Ndc80–tdTomato, shown in magenta. Kinetochores overlapping with the spindle appear white. In the drawings, microtubules are represented in green, and the lost kinetochore in magenta. Microtubule orientations and kinetochore positions from the previous images are marked with white dashed lines and white circles, respectively. The time after relieving cold stress is shown in minutes:seconds; scale bars, 1 μm. (**e**) Mean squared angular displacement (MSAD) of the microtubule. A linear fit with weights 1/s.e.m., $\mathrm{MSAD} = 2D_{\mathrm{MT}}\Delta t + \text{offset}$, yields $D_{\mathrm{MT}} = 3.3 \pm 0.1$ degrees^2 s^{-1}. Note that with the measured D_{MT}, microtubules cover on average $\Delta\alpha \approx 35°$ during their lifetime (3 min), but in principle, $\Delta\alpha$ can take values above 360° if a microtubule performs more than a full revolution. Microtubules of length 1–2 μm were used, $n = 106$. Grey denotes the area corresponding to subpixel movement of the plus end of a 1.5-μm-long microtubule. One-minute-long time series of α were used; error bars represent s.e.m. (strain AH01). The scheme indicates the angle used for the MSAD calculation. (**f**) Mean squared displacement (MSD) of the kinetochore. A linear fit, similar to that in Fig. 1e, yields $D_{\mathrm{KC}} = (5.9 \pm 0.3) \times 10^{-4}$ μm^2 s^{-1} ($n = 92$). Kinetochores were tracked with subpixel precision (Methods). Grey denotes the area corresponding to subpixel movement of the kinetochore. One-minute-long tracks were used; error bars represent s.e.m. (strains KI061 and AH01). The scheme represents a lost kinetochore trajectory. D_{KC} and D_{MT} refer to kinetochores and microtubules, respectively.

revealed that polar microtubules, which are straight, change their orientation with respect to the cell and to the spindle, where one end of the microtubule is attached to the SPB and the other end moves in the nucleoplasm[16] (Fig. 1c,d and Supplementary Videos S1 and S2). This pivoting of the microtubules around the SPB changes the distance between the microtubules and the lost kinetochore. After some time, the distance between one of the microtubules and the lost kinetochore diminishes, which is followed by retrieval of the kinetochore towards the SPB. Capture of the lost kinetochore is defined as the moment the retrieval starts. Kinetochores were captured by the microtubules extending from either SPB: 76% of the kinetochores were captured by a microtubule extending from the SPB that was closer to the kinetochore at the moment of capture ($n = 58$ out of 76 capture events), and 24% by a microtubule extending from the farther SPB ($n = 18/76$). The capture of the kinetochore occurred typically close to the microtubule tip ($n = 29/38$ attachments <500 nm away from the tip; Fig. 1c and Supplementary Video S1), but capture away from the tip was also observed ($n = 9/38$ attachments >500 nm away from the tip; Fig. 1d and Supplementary Video S2), as in budding yeast[20]. Out of 28 events where the behaviour of the microtubule before capture was observed, 27 microtubules pivoted and 1 microtubule grew directly towards the kinetochore. These findings suggest that pivoting of polar microtubules may play a significant role in finding lost kinetochores.

To understand the biological function of microtubule pivoting, it is important to quantify this process, which has not been done in any cell type so far. We investigated time series of the angle of the polar

Table 1 Microtubule and kinetochore behaviour measured in cells exposed to different temperatures.

Parameter	14 °C	24 °C	32 °C
Angular diffusion coefficient of the microtubule, D_{MT}, (degrees^2 s^{-1})	1.7 ± 0.1 (n = 101)	3.3 ± 0.1 (n = 106)	3.6 ± 0.2 (n = 101)
Diffusion coefficient of the kinetochore, D_{KC}, (μm^2 s^{-1})*	3.1 ± 0.1 × 10^{-4} (n = 42)	5.9 ± 0.3 × 10^{-4} (n = 92)	14.6 ± 0.9 × 10^{-4} (n = 45)
Microtubule length, L, (μm)†	1.2 ± 0.4 (n = 331)	1.5 ± 0.5 (n = 125)	1.5 ± 0.5 (n = 141)
Number of microtubules‡, n	3.3 ± 1.1 (n = 99)	2.6 ± 1.2 (n = 174)	3.4 ± 1.6 (n = 59)
Microtubule lifetime (min)§, T	12.6 ± 2.1 (n = 168)	3.0 ± 0.3 (n = 150)	3.9 ± 0.4 (n = 206)
Growth velocity (μm min^{-1})‖, v_g	1.6 ± 1.3 (n = 4)	2.7 ± 0.9 (n = 38)	1.5 ± 1.0 (n = 8)
Shrinkage velocity (μm min^{-1})¶, v_s	2.3 ± 1.5 (n = 8)	3.8 ± 2.1 (n = 47)	3.2 ± 1.3 (n = 4)
Initial distance of the kinetochore to the closer SPB, r_{KC} (t = 0), (μm)#	1.4 ± 0.6 (n = 256)	1.1 ± 0.4 (n = 333)	1.1 ± 0.4 (n = 361)
Size of the nucleus, 2R (μm)**		3.1 ± 0.4 (n = 13)	
Size of the kinetochore, a (μm)		0.2 (taken from ref. 34)	

Data are given as mean ± s.d. *For comparison, the diffusion coefficient of GFP in the nucleus, measured by fluorescence recovery after photobleaching (FRAP) experiments at 24 °C, was 5.6±2.8 μm^2 s^{-1} (Supplementary Fig. S5d). †Microtubule length was measured using live-cell images taken 4 min after cold treatment. Polar microtubules are often a bundle of a few microtubules of different length, as can be seen by a decrease of tubulin–GFP intensity towards the microtubule tip (Fig. 1d), which may lead to an underestimate of microtubule length by several hundred nanometres. ‡The number of microtubules per cell was measured in cells with lost kinetochores using live-cell images taken 2, 3, and 4 min after cold treatment. §Lifetime was calculated as the total observation time of all microtubules (schematically shown by the blue, orange, yellow and black curves in Supplementary Fig. S2f) divided by the number of events when a complete shrinkage of the microtubule was observed (blue and yellow curves in Supplementary Fig. S2f). The total observation time was the time interval in which each microtubule was observed, summed over all microtubules. The error on the microtubule lifetime was calculated as the lifetime divided by the square root of the number of observed catastrophe events, assuming a Poisson process. ‖Microtubule growth velocity was calculated as the slope of a linear fit of microtubule length as a function of time. The plus-end of the microtubule labelled with Mal3–GFP and the SPB labelled with Sid4–GFP were tracked automatically with subpixel resolution (strain YC001). ¶Shrinkage velocity was calculated from a similar fit as for growth, using manual tracking of microtubules labelled with GFP (strain KI061). #Initial distance of the kinetochore to the closer SPB was measured using samples fixed in methanol immediately after cold treatment. Methanol fixation preserved GFP and tdTomato signal but induced shrinkage of cells (about 28%); thus, the measured distance was corrected to take this effect into account. **The size of the nucleus, which had an elongated shape as a consequence of cell synchronization (Methods), was measured along its short axis. The size of the nucleus along the long axis was 6.0 ± 0.5 μm. The corresponding nuclear volume was in agreement with ref. 35.

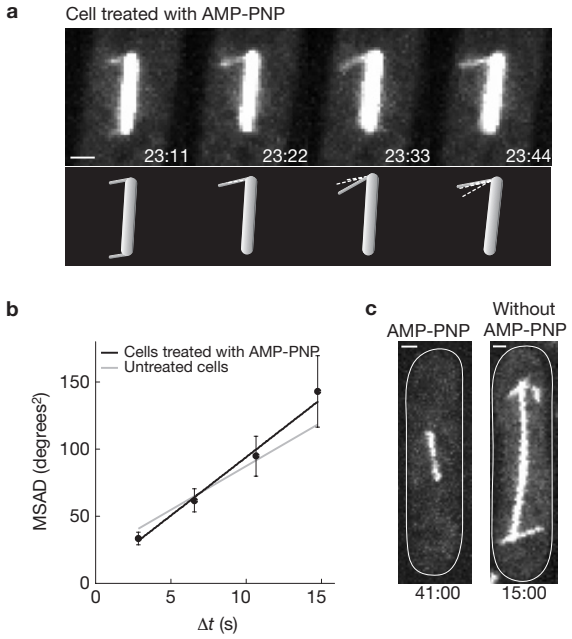

Figure 2 The pivoting motion of microtubules does not depend on ATP. (**a**) Time-lapse images and the corresponding drawings of microtubules in cells treated with 50 mM AMP-PNP (permeabilized by Triton X-100, see Methods; strain KI061 from Supplementary Table S1). In the drawings, microtubule orientations from the previous images are marked with white dashed lines. The time from the beginning of the AMP-PNP treatment is given in minutes:seconds. (**b**) Mean squared angular displacement (MSAD) of the microtubules in cells treated with AMP-PNP (strain KI061). A linear fit with weights 1/s.e.m., MSAD = 2$D_{MT}\Delta t$ + offset, yields D_{MT} = 4.4±0.7 degrees^2 s^{-1} (black line). Thirty-second-long time series of α of microtubules of length 0.75–2 μm were used (microtubule length was 1.2±0.3 μm, mean ± s.e.m., n = 27); error bars represent s.e.m. The fit from Fig. 1e for untreated cells is redrawn for comparison (grey line). (**c**) Image of the AMP-PNP-treated cell from **a**, taken 41 min after the beginning of the AMP-PNP treatment, when the spindle was 3 μm long, showing that spindle elongation was inhibited (left). Image of a control cell (without AMP-PNP), taken 15 min after the time when the spindle was 3 μm long, showing normal spindle elongation (right). The control cell was treated with Triton X-100 (see Methods) 30 min before the image was taken. The time is given in minutes:seconds; scale bars, 1 μm.

microtubule with respect to the orientation of the microtubule at the moment of capture, denoted α (inset in Fig. 1e and Supplementary Fig. S2a). As the presence of a lost kinetochore may affect the pivoting of polar microtubules, we investigated whether there is a difference in the pivoting between three groups of polar microtubules: those that eventually captured a lost kinetochore, those that did not capture a lost kinetochore, and polar microtubules in cells without a lost kinetochore. We found a similar angular displacement over 30 s for those three groups of polar microtubules (Supplementary Fig. S2b); thus, we conclude that the movement of polar microtubules is not influenced by the presence of lost kinetochores. In addition, the angular movement of the microtubules in cells with the microtubule plus-end protein Mal3 (refs 21,22) tagged with GFP, which were not exposed to cold stress, was similar to that in cold-treated cells with tubulin–GFP (Supplementary Fig. S2c and Video S3). To distinguish whether microtubule pivoting is directed or random, we calculated the mean squared angular displacement[23], and found that it scales linearly with time (Fig. 1e and see Supplementary Fig. S2d for individual microtubules and S2e for longer timescales). Such a linear relationship is characteristic of random movement, and from the slope we calculated the corresponding angular diffusion coefficient of microtubules (Table 1). Taken together, our results suggest that the angular movement of microtubules is random.

The observed angular movement of polar microtubules may be driven by thermal fluctuations or by active components such as motor proteins. To determine whether ATP-driven motor activity drives microtubule movement, we inhibited ATP-dependent processes by using AMP-PNP (adenylyl-imidodiphosphate), a non-hydrolysable ATP analogue. We observed that, even though motors were inhibited, polar microtubules exhibited angular movement similar to that in untreated cells (Fig. 2a,b and Supplementary Fig. S2c and Video S4). Motor inhibition was confirmed by the observation that spindles did not elongate[24,25] (Fig. 2c; Methods). These results show that the angular movement of microtubules is not driven by motor proteins, but most likely by thermal fluctuations. For thermally driven motion, theory predicts that the angular diffusion coefficient of the microtubule decreases with increasing microtubule length[26–28] (Supplementary Note S1). Our measurements of microtubule angular movement

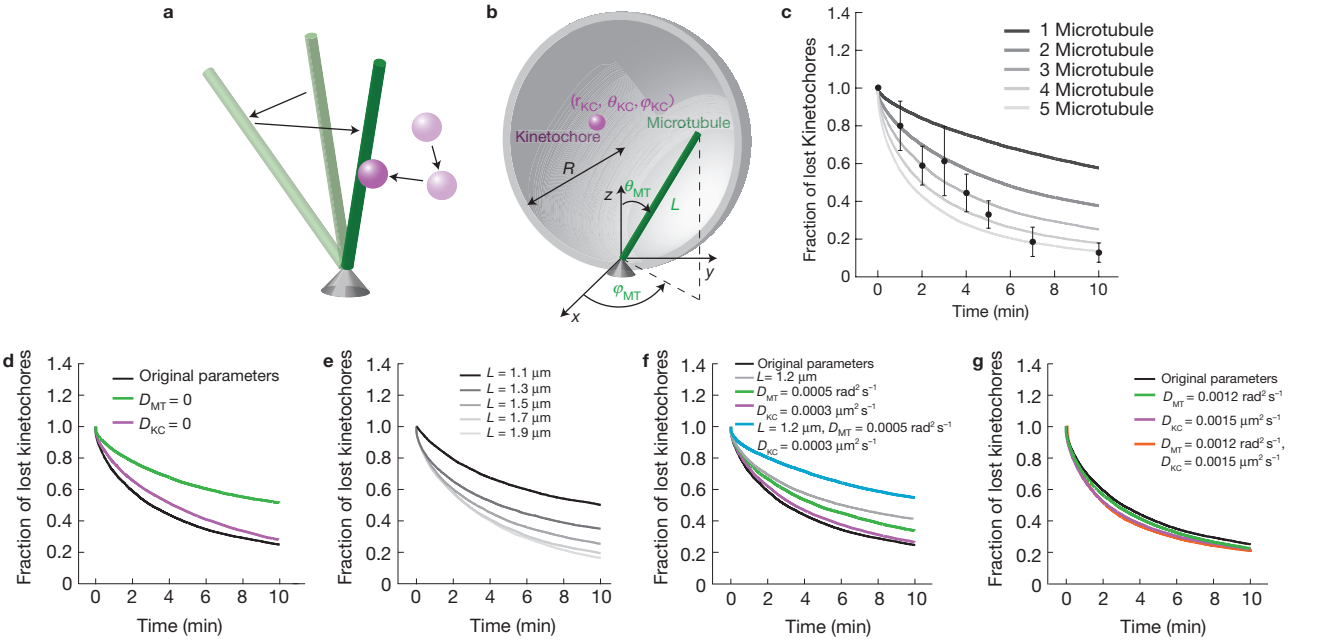

Figure 3 The model for kinetochore capture based on random angular movement of the microtubule and random movement of the kinetochore. (**a**) A polar microtubule (green) explores the space by pivoting around the SPB (grey cone). At the same time, a kinetochore (magenta) diffuses. Darker colours represent the moment of capture and lighter colours depict previous positions. (**b**) Geometry of the model. The microtubule (green) is a thin stiff rod freely jointed to the SPB (grey cone), which is on the nuclear envelope (grey half-sphere). The microtubule and the kinetochore (magenta) coordinates are explained in Supplementary Note S2. (**c**) Comparison of theoretical predictions and experimental measurements for the fraction of lost kinetochores as a function of time. Five theoretical curves are shown for $n = 1$–5 microtubules; parameters $D_{MT} = 10^{-3}$ rad^2 s^{-1}, $D_{KC} = 6 \times 10^{-4}$ μm^2 s^{-1} and $L = 1.5$ μm were measured here; r_{KC} (t = 0) is taken to be 1.2 μm (mean value of all experiments); $R = 1.5$ μm and $a = 0.2$ μm are taken from the literature (Table 1). The experimental data (points with error bars) are redrawn from Fig. 1b. (**d**) The effect of microtubule and kinetochore diffusion on the capture process. All parameters are as in **c** including $n = 3$ microtubules, termed original parameters (black). The green and magenta curves show results for the original parameters except $D_{MT} = 0$ and $D_{KC} = 0$, respectively. (**e**) The effect of microtubule length on the capture process. The curve for $L = 1.5$ μm corresponds to the original parameters, whereas the other curves correspond to different microtubule lengths (see legend). (**f**) The effect of low-temperature parameters. Results are shown: in black, for the original parameters; in green, magenta and grey for the original parameters except a single parameter, which is specified in the legend; in blue, for the original parameters except 3 parameters, see legend. The blue curve corresponds to low-temperature parameters, measured at 14 °C (Table 1). (**g**) The effect of high-temperature parameters. Results are shown: in black, for the original parameters; in green and magenta, for the original parameters except a single parameter, which is specified in the legend; in orange, for the original parameters except 2 parameters, see legend. The orange curve corresponds to high-temperature parameters, measured at 32 °C (Table 1).

as a function of microtubule length in cells expressing Mal3–GFP (Supplementary Fig. S3a and Video S3) were consistent with this prediction (Supplementary Fig. S3b).

To complete the picture of the behaviour of polar microtubules, we measured their number and dynamics (Table 1). There were, on average, 3 polar microtubules per cell at any time. Their growth rate, v_g, and shrinkage rate, v_s, were similar to those of interphase microtubules[18,29]. The life of an average microtubule consisted of growth to a length of $L = 1.5$ μm, a period of constant length, and shrinkage. Microtubules lived on average for 3 min, spending $L/v_g = 0.56$ min in the growth phase, $L/v_s = 0.39$ min in the shrinkage phase, and the remaining time of 2.05 min or roughly 70% of their lifetime in the phase of constant length. This calculation suggests that microtubule dynamics is slow, which was verified in measurements of microtubule length as a function of time (Supplementary Fig. S2g). This microtubule behaviour differs from that in interphase, where microtubules spend most of their lifetime in the growth phase.

In addition to the movement of polar microtubules, we observed the movement of lost kinetochores (Fig. 1c,d and Supplementary Videos S1 and S2) and of the spindle. Similarly to polar microtubules, kinetochores moved in a random manner before capture (Fig. 1f and Supplementary Fig. S4a,b, Table 1). To compare the extent of the random movement of the kinetochore and microtubule, we measured their displacement in 30 s. A kinetochore covers on average 0.2 μm, and the tip of a 1.5 μm long polar microtubule covers 0.4 μm by random angular movement of the microtubule. The kinetochore and the polar microtubule, therefore, explore a comparable fraction of space. In contrast, the movement of the spindle is negligible[30] (Supplementary Fig. S2h). Taken together, our results indicate that the movement of the lost kinetochore, as well as of the polar microtubules, plays a role for kinetochore capture.

To examine whether the process of kinetochore capture could be driven by the observed random movement of polar microtubules and the kinetochore (Fig. 3a), we develop a simple stochastic model. In our three-dimensional description, which is depicted in Fig. 3b, microtubules are thin stiff rods of fixed length performing angular diffusion around the SPB. Kinetochores are described as objects performing three-dimensional diffusion (Supplementary Note S2). When we include only one microtubule in the model, 25% of the lost kinetochores are captured in 4 min (Fig. 3c). Thus, our model

predicts that even a single microtubule can capture kinetochores at a timescale relevant for mitosis. When we include 3 microtubules as we measured experimentally, the capture process predicted by the model speeds up, giving the values that agree quantitatively with the experimentally measured fraction of lost kinetochores (Fig. 3c; P values for $n = 1$–5 microtubules are shown in Supplementary Table S2). The small discrepancy at longer times may be caused by underestimated microtubule length (Table 1). As our model does not have free parameters, the agreement between the typical capture time predicted by the model and the one measured experimentally directly supports our hypothesis that the process of kinetochore capture is driven by random movement of polar microtubules and of the kinetochore.

Our model predicts that the capture process depends mainly on the angular diffusion coefficient of the microtubule and on microtubule length (Fig. 3d,e), whereas the diffusion coefficient of the kinetochore (Fig. 3d), the size of the kinetochore (Supplementary Fig. S5a) and the size of the nucleus (Supplementary Fig. S5b) have a smaller effect. To test this prediction, we perturbed the behaviour of the microtubules and kinetochores experimentally by changing the temperature at which the process of kinetochore capture occurs. We expected the diffusion coefficient of the microtubule and kinetochore to change with temperature, as a result of changes in the viscosity of the nucleoplasm and other aspects such as chromosome condensation, as was shown for diffusion of other structures in the nucleus[31,32]. When we decreased the temperature from 24 to 14 °C, we observed a 50% reduction in both microtubule and kinetochore diffusion, as well as 20% reduced microtubule length (Table 1 and Supplementary Figs S2i and S4c). On the other hand, temperature increase to 32 °C did not change microtubule length but resulted in 150% increased kinetochore diffusion and 20% increased microtubule diffusion (Table 1 and Supplementary Figs S2i and S4c). For the two sets of parameters, corresponding to low temperature (14 °C) and high temperature (32 °C), the model predicts significantly slower and slightly faster capture, respectively, in comparison with the original set of parameters corresponding to 24 °C (Fig. 3f,g). The reason for the significant slowdown of the capture process predicted by the model is the smaller microtubule length and lower microtubule diffusion (Fig. 3f). For high-temperature parameters, on the other hand, the model predicts that the capture process speeds up only slightly because neither the 150% higher kinetochore diffusion nor the 20% higher microtubule diffusion affects the capture process significantly (Fig. 3g). Indeed, when we measured the kinetics of the capture process at 14 and 32 °C, the experimental results confirmed the predictions from the model (Fig. 4a,b; Supplementary Fig. S1 shows results of individual experiments; Supplementary Table S2 shows P values for $n = 1$–5 microtubules).

Finally, we investigated whether our model predicts that microtubule pivoting accelerates the search for kinetochores not only for parameters appropriate for fission yeast, but also for parameters that may be relevant for higher eukaryotic cells[9]. In human cells, kinetochore movement was quantified and shown to accelerate the search for kinetochores in a theoretical study[9]. Similarly, our model shows that kinetochore movement accelerates the search process (Supplementary Fig. S5c). Moreover, our model predicts for which range of the microtubule angular diffusion coefficient values, search by microtubule pivoting becomes relevant for higher eukaryotic cells (Supplementary Fig. S5c). Quantification of microtubule movements in higher eukaryotic cells will show to which extent microtubule pivoting helps the search for kinetochores.

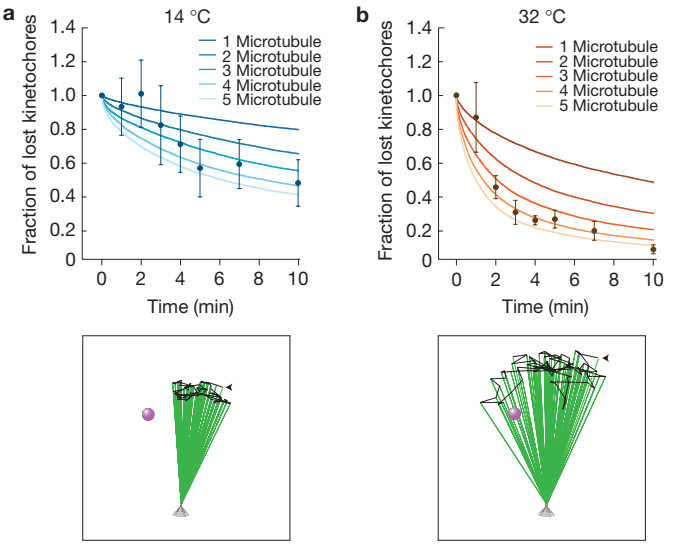

Figure 4 Comparison between theoretical predictions and experimental data. (**a**,**b**) Top, theoretical curves for 2 sets of parameters: $D_{MT} = 0.5 \times 10^{-3}$ rad^2 s^{-1}, $D_{KC} = 3 \times 10^{-4}$ μm^2 s^{-1}, $L = 1.2$ μm (**a**) and $D_{MT} = 1.2 \times 10^{-3}$ rad^2 s^{-1}, $D_{KC} = 15 \times 10^{-4}$ μm^2 s^{-1}, $L = 1.5$ μm (**b**), which were experimentally measured at 14 and 32 °C, respectively (Table 1). The remaining parameters are as in Fig. 3c. In each panel, 5 theoretical curves are shown for $n = 1$–5 microtubules. Points with error bars (mean ± s.e.m.), calculated as in Fig. 1b, represent the experimental data. The number of experiments was 8 and 11 at 14 and 32 °C, respectively (strains KI061 and AH01 from Supplementary Table S1; see also Supplementary Fig. S1). Bottom, drawings showing the orientations of a single microtubule during 4 min at 3-s intervals obtained by numerically solving equations (1) and (2) (Supplementary Note S2), using the same D_{MT} and L values as in the respective panels above. The initial microtubule orientation is marked by the arrowhead; the trace of the plus end is depicted by the black line. Note that the microtubule on the right explored more space and thus had a higher chance to capture the kinetochore.

We found that microtubules pivot around the SPB in a random manner and thereby explore the intranuclear space. We propose that the random movement of microtubules and kinetochores accelerates the search for kinetochores. Here we ask how long it would take for microtubules to capture kinetochores in fission yeast in a hypothetical case without microtubule pivoting. In this case, only those microtubules that grow towards the kinetochore can hit and capture the kinetochore. In the geometry representing the fission yeast nucleus (Fig. 3b), the kinetochore covers 1/100 of all directions in which microtubules can grow. This means that 1 out of 100 microtubules would directly hit the kinetochore. With the microtubule number and lifetime measured here, it would take 100 min for a cell to generate 100 microtubules and thus to capture the kinetochore (see also ref. 33). Yet, we measured that kinetochore capture occurs in 3–4 min (Fig. 1b). Compared with the scenario where microtubules do not pivot but directly hit the kinetochore, our theory shows that microtubule pivoting accelerates the search for kinetochores in the geometry of the fission yeast nucleus by 1–2 orders of magnitude.

Pivoting of the microtubules and the movement of kinetochores may drive, in addition to kinetochore capture in mitosis, spindle assembly including kinetochore capture in both mitosis and meiosis in yeasts and

similar cells. In some of these processes, microtubule dynamics and the geometry in which microtubules extend from two spindle poles may be necessary to explain the dynamics of the process, which was not the case for the kinetochore capture studied here. Our theory can be extended by including two spindle poles and dynamic microtubules, to explore spindle assembly including kinetochore capture in mitosis and meiosis in various cells, as well as to describe kinetochore capture in fission yeast in more detail. In general, it will be interesting to investigate how microtubules, by moving laterally, locate targets in various cellular contexts. □

METHODS

Methods and any associated references are available in the online version of the paper.

Note: Supplementary Information is available in the online version of the paper

ACKNOWLEDGEMENTS

We thank K. Sawin, A. Haese, Y. Caldarelli, E. Guarino, S. Kearsey and the Yeast Genetic Resource Center for strains and plasmids; B. Schroth-Diez from the Light Microscopy Facility of MPI-CBG for help with microscopy; I. Šarić for the drawings; W. Zachariae, S. Grill, J. Howard, D. Cimini, J. Gregan, M. Žanić, E. Paluch, N. Maghelli, M. Coelho and V. Ananthanarayanan for discussions and advice; the German Research Foundation (DFG) and the Human Frontier Science Program (HFSP) for financial support. M.R.C. was supported by a Marie Curie Intra-European Fellowship and D.R-J. by a Humboldt Research Fellowship for Postdoctoral Researchers.

AUTHOR CONTRIBUTIONS

I.K. carried out all experiments and data analysis, A.N. performed simulations, P.D., M.R.C. and A.H.K. carried out AMP-PNP and FRAP experiments, D.R-J. analysed the data shown in Supplementary Fig. S3b, A.K. developed the tracking software, B.L. and N.P. developed the theory, and I.M.T-N. and N.P. designed the project and wrote the paper.

COMPETING FINANCIAL INTERESTS

The authors declare no competing financial interests.

Published online at www.nature.com/doifinder/10.1038/ncb2640
Reprints and permissions information is available online at www.nature.com/reprints

1. Cheeseman, I. M. & Desai, A. Molecular architecture of the kinetochore-microtubule interface. *Nat. Rev. Mol. Cell Biol.* **9,** 33–46 (2008).
2. Mitchison, T. J. & Kirschner, M. W. Properties of the kinetochore *in vitro*. II. Microtubule capture and ATP-dependent translocation. *J. Cell Biol.* **101,** 766–777 (1985).
3. Hill, T. L. Theoretical problems related to the attachment of microtubules to kinetochores. *Proc. Natl Acad. Sci. USA* **82,** 4404–4408 (1985).
4. Holy, T. E. & Leibler, S. Dynamic instability of microtubules as an efficient way to search in space. *Proc. Natl Acad. Sci. USA* **91,** 5682–5685 (1994).
5. Carazo-Salas, R. E. *et al.* Generation of GTP-bound Ran by RCC1 is required for chromatin-induced mitotic spindle formation. *Nature* **400,** 178–181 (1999).
6. Wollman, R. *et al.* Efficient chromosome capture requires a bias in the 'search-and-capture' process during mitotic-spindle assembly. *Curr. Biol.* **15,** 828–832 (2005).
7. Witt, P. L., Ris, H. & Borisy, G. G. Origin of kinetochore microtubules in Chinese hamster ovary cells. *Chromosoma* **81,** 483–505 (1980).
8. Kitamura, E. *et al.* Kinetochores generate microtubules with distal plus ends: their roles and limited lifetime in mitosis. *Dev. Cell* **18,** 248–259 (2010).
9. Paul, R. *et al.* Computer simulations predict that chromosome movements and rotations accelerate mitotic spindle assembly without compromising accuracy. *Proc. Natl Acad. Sci. USA* **106,** 15708–15713 (2009).
10. Burbank, K. S., Groen, A. C., Perlman, Z. E., Fisher, D. S. & Mitchison, T. J. A new method reveals microtubule minus ends throughout the meiotic spindle. *J. Cell Biol.* **175,** 369–375 (2006).
11. Mahoney, N. M., Goshima, G., Douglass, A. D. & Vale, R. D. Making microtubules and mitotic spindles in cells without functional centrosomes. *Curr. Biol.* **16,** 564–569 (2006).
12. Mogilner, A. & Craig, E. Towards a quantitative understanding of mitotic spindle assembly and mechanics. *J. Cell Sci.* **123,** 3435–3445 (2010).
13. O'Connell, C. B. & Khodjakov, A. L. Cooperative mechanisms of mitotic spindle formation. *J. Cell Sci.* **120,** 1717–1722 (2007).
14. Duncan, T. & Wakefield, J. G. 50 ways to build a spindle: the complexity of microtubule generation during mitosis. *Chromosome Res.* **19,** 321–333 (2011).
15. Funabiki, H., Hagan, I., Uzawa, S. & Yanagida, M. Cell cycle-dependent specific positioning and clustering of centromeres and telomeres in fission yeast. *J. Cell Biol.* **121,** 961–976 (1993).
16. Sagolla, M. J., Uzawa, S. & Cande, W. Z. Individual microtubule dynamics contribute to the function of mitotic and cytoplasmic arrays in fission yeast. *J. Cell Sci.* **116,** 4891–4903 (2003).
17. Zimmerman, S., Daga, R. R. & Chang, F. Intra-nuclear microtubules and a mitotic spindle orientation checkpoint. *Nat. Cell Biol.* **6,** 1245–1246 (2004).
18. Gachet, Y. *et al.* Sister kinetochore recapture in fission yeast occurs by two distinct mechanisms, both requiring Dam1 and Klp2. *Mol. Biol. Cell* **19,** 1646–1662 (2008).
19. Grishchuk, E. L. & McIntosh, J. R. Microtubule depolymerization can drive poleward chromosome motion in fission yeast. *EMBO J.* **25,** 4888–4896 (2006).
20. Tanaka, K. *et al.* Molecular mechanisms of kinetochore capture by spindle microtubules. *Nature* **434,** 987–994 (2005).
21. Beinhauer, J. D., Hagan, I. M., Hegemann, J. H. & Fleig, U. Mal3, the fission yeast homologue of the human APC-interacting protein EB-1 is required for microtubule integrity and the maintenance of cell form. *J. Cell Biol.* **139,** 717–728 (1997).
22. Busch, K. E. & Brunner, D. The microtubule plus end-tracking proteins mal3p and tip1p cooperate for cell-end targeting of interphase microtubules. *Curr. Biol.* **14,** 548–559 (2004).
23. Berg, H. C. *Random Walks in Biology* (Princeton Univ. Press, 1993).
24. Masuda, H., Hirano, T., Yanagida, M. & Cande, W. Z. *In vitro* reactivation of spindle elongation in fission yeast nuc2 mutant cells. *J. Cell Biol.* **110,** 417–425 (1990).
25. Lee, G. M. Characterization of mitotic motors by their relative sensitivity to AMP-PNP. *J. Cell Sci.* **94,** 425–441 (1989).
26. Broersma, S. Rotational diffusion constant of a cylindrical particle. *J. Chem. Phys.* **32,** 1626–1631 (1960).
27. Hunt, A. J., Gittes, F. & Howard, J. The force exerted by a single kinesin molecule against a viscous load. *Biophys. J.* **67,** 766–781 (1994).
28. Tirado, M. M. & de la Torre, J. G. Translational friction coefficients of rigid, symmetric top macromolecules. Application to circular cylinders. *J. Chem. Phys.* **71,** 2581–2587 (1979).
29. Drummond, D. R. & Cross, R. A. Dynamics of interphase microtubules in *Schizosaccharomyces pombe*. *Curr. Biol.* **10,** 766–775 (2000).
30. Vogel, S. K., Raabe, I., Dereli, A., Maghelli, N. & Tolic-Norrelykke, I. Interphase microtubules determine the initial alignment of the mitotic spindle. *Curr. Biol.* **17,** 438–444 (2007).
31. Gehlen, L. R. *et al.* Nuclear geometry and rapid mitosis ensure asymmetric episome segregation in yeast. *Curr. Biol.* **21,** 25–33 (2011).
32. Shav-Tal, Y. *et al.* Dynamics of single mRNPs in nuclei of living cells. *Science* **304,** 1797–1800 (2004).
33. Gopalakrishnan, M. & Govindan, B. S. A first-passage-time theory for search and capture of chromosomes by microtubules in mitosis. *Bull. Math. Biol.* **73,** 2483–2506 (2011).
34. Ding, R., McDonald, K. L. & McIntosh, J. R. Three-dimensional reconstruction and analysis of mitotic spindles from the yeast, *Schizosaccharomyces pombe*. *J. Cell Biol.* **120,** 141–151 (1993).
35. Neumann, F. R. & Nurse, P. Nuclear size control in fission yeast. *J. Cell Biol.* **179,** 593–600 (2007).

DOI: 10.1038/ncb2640

METHODS

Strains and gene tagging. Amino-terminal epitope tagging of ndc80 with tdTomato was performed by using a polymerase chain reaction (PCR) gene-targeting method[36]. Using this method the open reading frame of the tdTomato under the nmt41 (thiamine regulated) promoter was integrated into the original gene locus by homologous recombination. The primers were designed using the web tool http://www.bahlerlab.info/resources/ (ref. 37): forward primer: 5′-TTGCGGTTCTATATTGGAAATCGCTATTCACTGTTATTTTTGTTACTTAGCAAAGTGGTTTTGTTGTTATAACTAACGTCGAATTCGAGCTCGTTTAAAC-3′; reverse primer: 5′-AATACCCTAAACTTATTGTTAACTTATTAGTCAAAAGAAAAAAAAGAAAACATACGCCTCGCGTAAGAGGAAGAATCTTGCTTGTACAGCTCGTCCATGCC-3′

The primers contain 80 base pairs homologous to the flanking sequences of ndc80 and 20 base pairs homologous to a template. As a template we used the plasmid pKS398 (pFA6a–kanMX6–P41nmt1–tdTomato), a gift from K. Sawin (University of Edinburgh, UK). DNA fragments including the nmt promoter sequence, the tdTomato sequence and the kanamycin cassette were PCR amplified. The strain FY8004 (obtained through YGRC from M. Yanagida, Okinawa Institute of Science and Technology, Japan) was transformed with the DNA fragments using a lithium-acetate method[38]. The obtained strain, KI006, was the parent strain for all subsequent strains, which also contain α-tubulin–GFP and Sid4–GFP (a protein of the SPB). The strains were obtained by crossing, followed by random spore analysis. The strain AH01 was created by A. Haese (Max Planck Institute of Molecular Cell Biology and Genetics, Germany), and the strain YC001 by Y. Caldarelli (Max Planck Institute of Molecular Cell Biology and Genetics, Germany).

Strains used for FRAP experiments were obtained by amplifying the nuclear localization sequence (NLS–GFP), from vector pSGP583 (SV40 NLS–GFP–lacZ; provided by S. Forsburg, University of Southern California, USA) with the primers: 5′-CGCGCTAGCGCCATGGCTCCTAAGAAGAAGCGTAAG-3′ and 5′-GCGCCCGGGGCTTATTTGTATAGTTCATCCATGCCAT-3′. Before ligation, the PCR product and the target vector pDUAL2–HFG1c (Riken Bioresource Centre) were digested with NheI/XmaI to obtain pDUAL2–nmt1–NLS–GFP (pAK06). DNA was confirmed by sequencing and a strain with uracil deficiency (FY13143, YGRC) was transformed by electroporation (PD31, Supplementary Table S1). Cells were selected on Edinburgh minimal medium (EMM) lacking uracil. For control FRAP experiments with cytoplasmic expression of GFP, the strain FY13143 was transformed by electroporation with pDUAL2–HFG1c (PD30, Supplementary Table S1) and selected on EMM plates lacking uracil.

Sample preparation. Strain YC001 was prepared for microscopy as follows. The cells were grown on Yeast Extract (YE) medium agar plates with appropriate supplements at room temperature (23–27 °C; ref. 38). Liquid pre-cultures were grown in EMM with appropriate supplements in a shaking incubator (ISF-1-W, Kuehner Shaker) at 25 °C. The pre-cultures were used to inoculate EMM containing appropriate supplements. Cells were grown to the exponential phase at 25 °C (OD600 ≈ 0.5) and 200 µl of cell culture was placed on the glass bottom of a 35 mm (No1.5) culture dish (MatTek Corporation) for 10 min for sedimentation. The cells attached to the glass bottom, which had been coated with lectin (L2380, Sigma-Aldrich). The cells were washed several times with EMM at room temperature and live-cell imaging was performed at room temperature (22–23 °C).

Cell synchronization. Cells containing a *cdc25-22* mutation (strains KI061 and AH01) were prepared as described above for strain YC001, except that the cells were grown to the exponential phase at 25 °C in EMM with appropriate supplements and 10 µM thiamine, and were subsequently grown for 4 h at 37 °C in EMM containing 5 µM thiamine. This led to accumulation of cells in G2, because the cdc25 gene function, required to initiate mitosis[39], was abolished by keeping the cells at a high temperature. To let the cells proceed into mitosis, the temperature of the cell culture was reduced to 25 °C. After 20–30 min, most cells were in metaphase. At that time spindles were 1–2 µm long and the kinetochores were between the SPBs.

Microtubule depolymerization by cold treatment. To decrease the temperature of the cell culture quickly, we applied cold treatment to a small volume of cell culture (5 µl). To get enough cells, the cell culture was centrifuged for 3 min at 2,900*g* (Heraeus multifuge 3 S-R, Thermo Electron Corporation). The supernatant was discarded and the cells were re-diluted in a small volume of EMM. Lectin-coated culture dishes (see above) were pre-cooled on ice. Subsequently, 5 µl of the cell culture was spread on the glass bottom of the culture dish and left on ice for 30 min (cold treatment). The cells attached to the glass bottom of the dish, and were washed several times with EMM at different temperatures (14, 24 or 32 °C), followed by live-cell imaging. It took 2–3 min to find a cell with a lost kinetochore and to start acquiring a movie. During imaging, cells were exposed to 14, 24 or 32 °C using a heating/cooling chamber (Warner Instruments).

Cell fixation. Experiments on fixed cells were performed as described above until the end of the cold treatment. The cells were then rewarmed to 14, 24 or 32 °C using a circulating water bath (Haake DC10-P5/U, Thermo Electron Corporation). Before imaging, the cells were fixed with methanol (20856.296, AnalaR Normapur, VWR International), cooled at −20 °C for at least 1 h. Cells were fixed directly in glass-bottom culture dishes, 35 mm No 1.5 (MatTek Corporation), for 1 h and then washed gradually (15 min in 30, 50, 70, 90 and 100% PEM in methanol). PEM buffer consisted of 0.1 M PIPES (P8203, Sigma-Aldrich), 5 mM EGTA (E4378, Sigma-Aldrich) and 2 mM $MgCl_2 \cdot 6H_2O$ (M0250, Sigma-Aldrich), adjusted to pH 6.8 using NaOH solution.

AMP-PNP treatment. KI061 cells were grown and prepared for microscopy as described above. The cell culture (100 µl) was placed in a culture dish. Experiments were performed at 24 °C on either synchronized or unsynchronized cells. Cells were permeabilized for 10 min with 0.3% Triton X-100 in EMM with appropriate supplements, and then washed 3 times with EMM with supplements. AMP-PNP (50 mM; Roche) dissolved in EMM with supplements was added and time-lapse live-cell imaging (see below) started 10–20 min after AMP-PNP addition. The cells were imaged every 2–3 s for 15 min to follow the movement of polar microtubules, and subsequently every 2 min for 15 min to measure spindle elongation. Only the spindles that elongated by <1 µm in >30 min of AMP-PNP treatment, which was the case in 60% of cells, were used for measurements of microtubule movement. For comparison, untreated spindles elongate by ∼7 µm in 30 min (ref. 30). To test for cell survival after the experiment, time-lapse images were taken for 10 min by using bright-field microscopy. These images showed no significant changes in cell appearance after Triton X-100 treatment and/or 40–60 min of AMP-PNP treatment. As a further control, we washed out AMP-PNP in 29 cells and observed that 16 spindles resumed elongating after the wash-out, whereas the remaining 13 spindles did not elongate. Thus, most of the cells were alive after the treatments with Triton X-100 and AMP-PNP and their spindles were functional.

Time-lapse live cell imaging. Live-cell images were taken using an Andor Revolution Spinning Disk System (Andor Technology), consisting of a Yokogawa CSU10 spinning-disc scan head (Yokogawa Electric Corporation) with a 405/488/568/647 Yokogawa dichroic beam splitter (Semrock). The scan head was connected to an Olympus IX71 inverted microscope (Olympus) equipped with a fast piezo objective *z*-positioner (PIFOC, Physik Instrumente GmbH & K.G.) and an Olympus UPlanSApo ×100/1.4 NA oil objective (Olympus). For cells expressing GFP and tdTomato, we performed sequential imaging (2 s time interval between each image pair) or simultaneous acquisition (1 s time interval between images) using a DualView image splitter (Optical Insights, Photometrics). Cells expressing only GFP (Mal3–GFP) were imaged with a 250 ms time interval. The exposure time was 20 ms. For excitation, a sapphire 488 nm solid-state laser (75 mW; Coherent) and a Jive 561 nm solid-state laser (75 mW; Cobolt) were used for GFP and tdTomato, respectively. The laser intensity was controlled using the acousto-optic tunable filter inside the Andor Revolution Laser Combiner (ALC, Andor Technology). For sequential imaging, the emission wavelength was selected using respective emission filters BL 525/30 (Semrock) and ET 605/70 (Chroma) mounted in a fast, motorized filter wheel (Lambda-10B, Sutter Instrument Company). For simultaneous imaging, the DualView image-splitter was equipped with a BL 525/40 (Semrock), a BS 565 (Chroma) and an ET 605/70 (Chroma). Stopped-disc and fluorescent bead (0.2 µm TetraSpec microspheres, T7280, Invitrogen, Molecular Probes) images were used for alignment of red and green channels. Images of neighbouring fields for experiments with methanol-fixed cells were performed using a motorized ProScanIII *x*–*y*-scanning stage (Prior Scientific Instruments). The microscope was equipped with an iXon EM+ DU-897 BV back-illuminated electron-multiplying CCD (charge-coupled device; Andor Technology), cooled to −80 °C, electron multiplication gain 300. The resulting *x*–*y*-pixel size in the images was 175 nm; the *z*-distance between optical sections was 500–600 nm. The system was controlled by Andor iQ software version 1.9.1 (Andor Technology).

FRAP. Pilot experiments were performed using strain 264 (leu1–32 ura4Δ [pRep3X–NLS–GFP]), provided by E. Guarino and S. Kearsey (University of Oxford, UK). Cells expressing NLS–GFP were attached to a glass-bottom dish with lectin (L2380, Sigma-Aldrich). Cells in mitosis were identified by their elongated nuclei. Experiments were performed at room temperature (22–24 °C) using an Andor Revolution Spinning Disk System (Andor Technology), consisting of a Yokogawa CSU-X1 spinning-disc scan head (Yokogawa Electric Corporation), connected to an Olympus IX81 inverted microscope (Olympus). The microscope was equipped with a Prior ProScanIII *x*–*y* scanning stage (Prior Scientific) and an Olympus UPlanSApo ×100/1.4 NA oil objective (Olympus). Excitation for imaging and bleaching was done using a sapphire 488 nm solid-state laser (50 mW; Coherent). The laser power was controlled using the acousto-optic tunable filter in the Andor

Revolution Laser Combiner (ALC, Andor Technology). The emission filter used was BL HC 525/30 (Semrock). The microscope was equipped with an iXon EM+ DU-897 BV back-illuminated electron-multiplying CCD camera, cooled to −80 °C(Andor Technology). The resulting x–y-pixel size in the images was 129 nm. The system was controlled by Andor iQ2 software version 2.6 (Andor Technology). A series of 50 single-plane time-lapse images was acquired before the bleaching step with a 50 ms exposure time and 10–15% of the 488 nm laser. Bleaching was then performed on a 2×2 pixel area with 50% of the 488 nm laser, with a dwell time of 1 ms and 2 repeats on each pixel. Following the bleaching, 400 single-plane images were acquired as before the bleaching. All of the observed cells survived the treatment and underwent division.

Image processing and data analysis. Measurements of microtubule and kinetochore positions were performed in the maximum-intensity projections of the z-stacks. We did not measure positions along the z axis because the corresponding point-spread function of the microscope is about 800 nm, which is roughly half of the length of a typical microtubule. We estimate the systematic error resulting from two-dimensional measurements in Supplementary Note S3. Maximum-intensity projections were calculated with ImageJ (National Institutes of Health) using the plug-in Stacks-Z-function—Grouped ZProjector. The colour-merge images were obtained by overlay of projections in green and red channels using the plug-in Colour functions—Colour merge. Microtubules labelled with GFP were tracked manually in the maximum-intensity projections using the plug-in Particle analysis—Manual tracking. Specialized software was developed to determine the kinetochore position in the maximum-intensity projections. The intensity in the image was assumed to be a combination of photons from a two-dimensional Gaussian and a uniform distribution. The Gaussian distribution represents the photons emitted by the kinetochore, and the uniform distribution represents the background. The optimal set of parameters for this system was defined as the most probable one with respect to the acquired image. An iterative algorithm was used to find the optimal parameters, with a user-provided initialization for the first frame. Final data analysis was performed using scripts written in MATLAB (The Mathworks).

36. Bahler, J. *et al*. Heterologous modules for efficient and versatile PCR-based gene targeting in *Schizosaccharomyces pombe*. *Yeast* **14,** 943–951 (1998).
37. Penkett, C. J., Birtle, Z. E. & Bahler, J. Simplified primer design for PCR-based gene targeting and microarray primer database: two web tools for fission yeast. *Yeast* **23,** 921–928 (2006).
38. Forsburg, S. L. & Rhind, N. Basic methods for fission yeast. *Yeast* **23,** 173–183 (2006).
39. Russell, P. & Nurse, P. cdc25+ functions as an inducer in the mitotic control of fission yeast. *Cell* **45,** 145–153 (1986).

DOI: 10.1038/ncb2640

nature cell biology

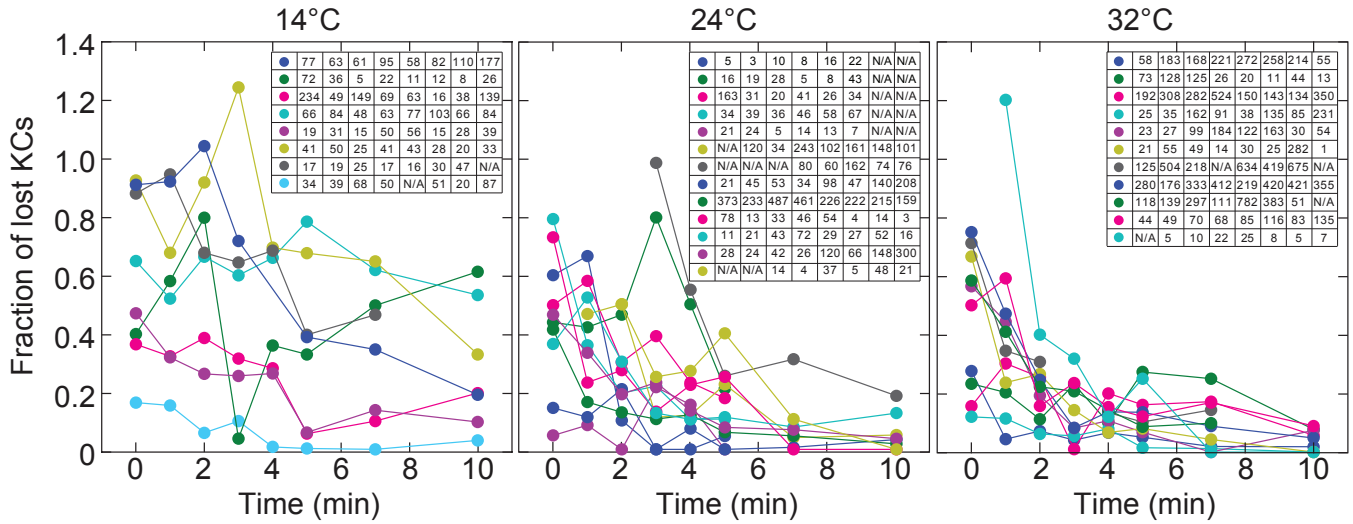

Figure S1 Fraction of lost KCs at different temperatures. Fraction of lost KCs as a function of time after relieving cold stress is shown for independent experiments, illustrating experimental variability. The temperature during spindle re-assembly and KC capture was, from left to right, 14°C, 24°C, and 32°C. The fraction of lost KCs was calculated as the number of lost KCs (n_{KC}) / number of cells in metaphase (n_{cells}). Independent experiments are shown in different colors. The number of metaphase cells for each time point in each experiment is shown in the corresponding color. Data were not acquired at 6, 8, and 9 minutes. N/A marks additional time points at which data were not acquired. To obtain the results shown in Fig. 1b, we averaged the data over all experiments at 24°C (n=13) and then normalized to obtain 1 lost KC per cell at time 0. The same procedure was followed in Fig. 4.

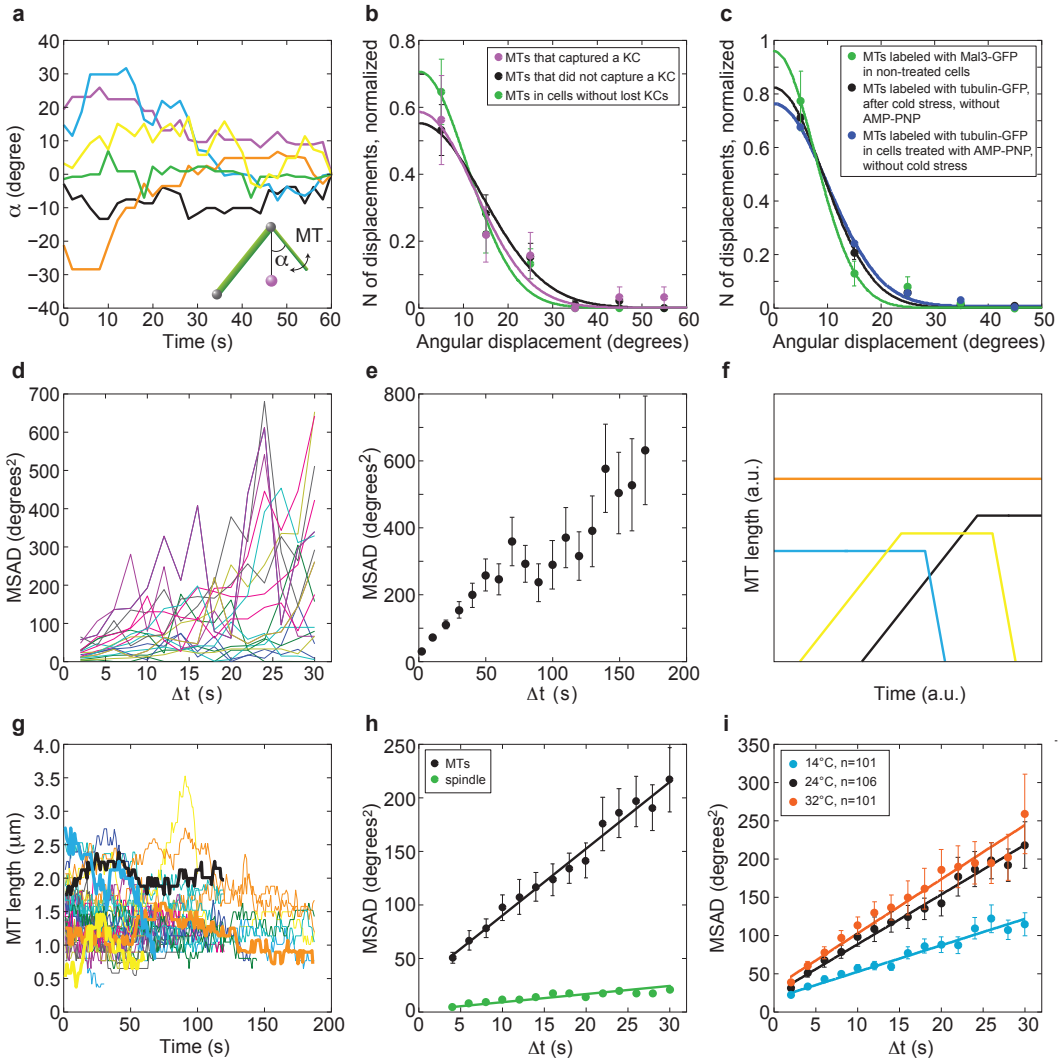

Figure S2 Angular movement of MTs. (**a**) Angle of the polar MT, a, during the last minute before KC capture, with respect to the orientation of the MT at the moment of capture. 6 MTs from different cells (strain AH01, Supplementary Table S1) are shown in different colors. (**b**) Angular displacement of MTs in 30 s, normalized to the total number of measurements. The data for the MTs that captured a KC (n=16 MTs, Group 1), those that did not capture a KC (n=46 MTs, Group 2), and MTs in cells without lost KCs (n=34 MTs, Group 3) is shown (points with error bars, which were calculated as the square root of the number of displacements in the bin divided by the total number of displacements). A Gaussian function, $y=a\cdot\exp(-x^2/(2\cdot c^2))$, was fitted to the data. The values of parameters a and c were 0.59 and 12.4, 0.55 and 14.2, 0.71 and 10.7 for Group 1, 2, and 3, respectively. A Mann-Whitney U-test showed that the data were not statistically different: p=0.9 for Group 1 versus 2, p=0.3 for Group 1 versus 3, and p=0.2 for Group 2 versus 3. (**c**) Angular displacement of MTs in 10 s, normalized to the total number of measurements. The length of all MTs was between 0.5 and 1.5 μm. The data for the MTs labeled with Mal3-GFP in untreated cells (n=62 MTs, Group 1), MTs labeled with tubulin-GFP in cells after cold stress without AMP-PNP (n=57 MTs, Group 2), and MTs labeled with tubulin-GFP in cells treated with 50 mM AMP-PNP without cold stress (n=44 MTs, Group 3) are shown (points with error bars, which were calculated as in panel b). The fits were performed as in panel b; a and c were 0.96 and 7.6 for Group 1, 0.82 and 9.2 for Group 2, 0.76 and 9.9 for Group 3. A Mann-Whitney U-test showed that data were not statistically different: p=0.6 for Group 1 versus 2, p=0.9 for Group 1 versus 3, and p=0.9 for Group 2 versus 3. (**d**) Mean squared angular displacement (MSAD) of independent MTs, randomly chosen from the set of 106 MTs analyzed in Fig. 1e. The plot illustrates the variability of movement between different MTs. 1 minute long time series of a were used, all MTs were 1-2 μm long. (**e**) MSAD of the MTs up to a time-lag of 3 minutes, showing that MSAD scales roughly linearly with time also on longer time scales. 3 minute long time series of a were used, all MTs were 1-2 μm long, error bars represent s.e.m., n=29 MTs. (**f**) Schematic representation of three different segments of MT life used for the calculation of MT lifetime in Table 1. The lifetime was calculated as the total observation time of all MTs (blue, orange, yellow and black curves) divided by the number of events when a complete shrinkage of the MT was observed (blue and yellow). The total observation time was the time interval in which each MT was observed, summed over all MTs, irrespective of whether the MT already existed at the beginning of the movie (blue and orange) or not (yellow and black), and whether shrinkage was observed (blue and yellow) or not (orange and black). (**g**) MT length over time in cells rewarmed after cold treatment (strain AH001, n=40 MTs). MTs that captured a lost KC are not included. 4 MTs that roughly correspond to those drawn in panel f are highlighted with thick lines. (**h**) MSAD of the MTs (n=106) and the spindle (n=26). The data for the MTs are redrawn from Fig. 1e. The mean length of the spindle was 3.5 μm. 1 minute long movies were used, error bars represent s.e.m. Error bars for the spindle overlap with the data points. (**i**) MSAD of the MTs from cells exposed to either 14°C, 24°C, or 32°C after cold treatment. Linear fits as in Fig. 1e are also shown. The resulting angular diffusion coefficients are reported in Table 1. For this analysis, only those MTs with the length close to the mean MT length at the corresponding temperature were used (1.2±0.5 μm at 14°C, and 1.5±0.5 μm at 24°C and 32°C). 1 minute long time series of a were used, error bars represent s.e.m. (strains KI061 and AH01).

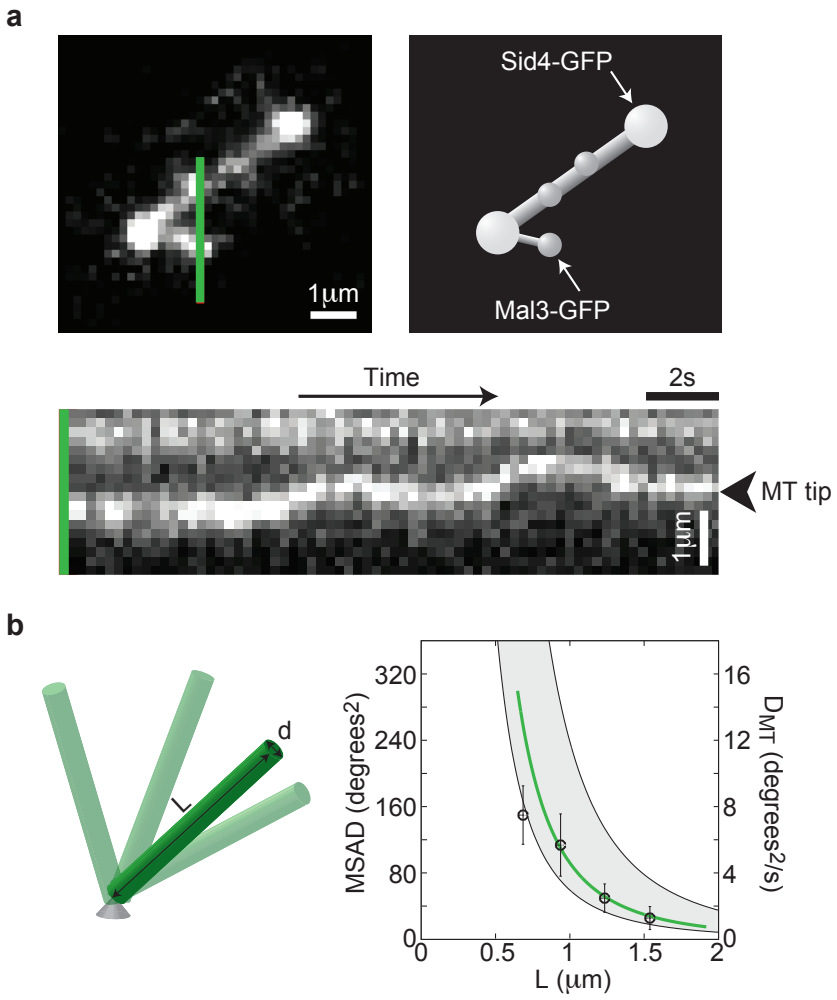

Figure S3 Dependence of the MT angular diffusion coefficient on MT length. (**a**) Image of a cell expressing Mal3-GFP and Sid4-GFP (top left; see Supplementary Movie S3; strain **YC001, Supplementary Table S1), the corresponding drawing (top right), and a kymograph (bottom) generated from Supplementary Movie 3 along the green line, visualizing the movement of the MT tip, which corresponds to the angular movement of the MT. (**b**) Left: A scheme of polar MT (green), which can be described as a thin stiff rod with one end freely jointed to a fixed point (grey cone, representing SPB). The other end of the rod is free to move, allowing the rod to perform angular movement. Examples of different positions of the rod are shown to visualize the degrees of freedom allowed by the free joint. Thermally driven angular diffusion of such a rod is described by D (degrees^2/s) = (3×180^2 ln(L/d) $k_B T$) / (4 π^3 L^3 h), where d is the diameter of the rod, k_B is the Boltzmann constant, T is absolute temperature, and h is the viscosity of the medium. This is a good approximation for L>>d (Refs.[1, 3]). Right: MSAD at Δt = 10 s as a function of the mean MT length <L> during the corresponding 10-s interval (strain YC001). The angular diffusion coefficient D = $MSAD$/(2×Δt) is shown on the axis at the right side. The number of data points in the bins was 39, 24, 16, 5, respectively; error bars represent s.e.m. A single-parameter fit of the equation given above to the data yielded the viscosity h = 2600 cP (green line). The grey area marks D of a cylinder in a medium with a viscosity of 1000 cP (upper bound) and 4000 cP (lower bound).

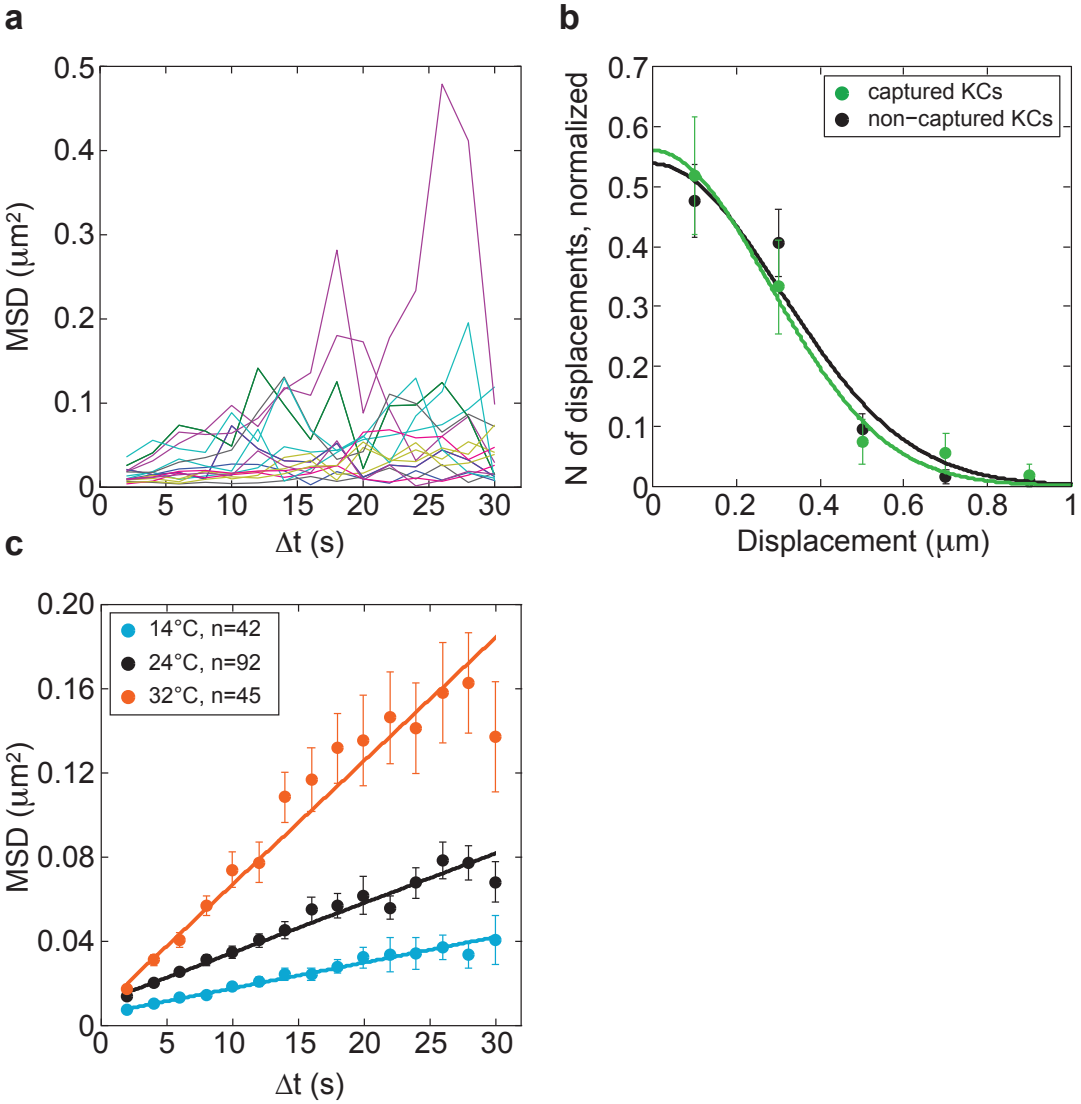

Figure S4 Movement of the KCs. (**a**) Mean squared displacement (MSD) of independent KCs, randomly chosen from the set of 92 KCs analyzed in Fig. 1f. The plot illustrates the variability of movement between different KCs. 1 minute long tracks were used (strains KI061 and AH01, Supplementary Table S1). (**b**) The displacement of lost KCs in 30 s, normalized to the total number of measurements. The displacement of lost KCs during the last minute before capture (n=27 KCs) and the displacement of lost KCs that were not captured until about 8 minutes after relieving cold stress (n=34 KCs) is shown (points with error bars, which were calculated as in Supplementary Fig. S2b). The fits were performed as in Supplementary Fig. S2b; a and c were 0.56 and 0.28 for lost KCs that were captured, 0.54 and 0.30 for lost KCs that were not captured. A Mann-Whitney U-test showed that the data were not statistically different (p=0.9). (**c**) MSD of the KCs in cells exposed to either 14°C, 24°C, or 32°C after cold treatment. Linear fits as in Fig. 1f are also shown. The resulting diffusion coefficients are reported in Table 1. 1 minute long tracks were used, error bars represent s.e.m. (strains KI061 and AH01).

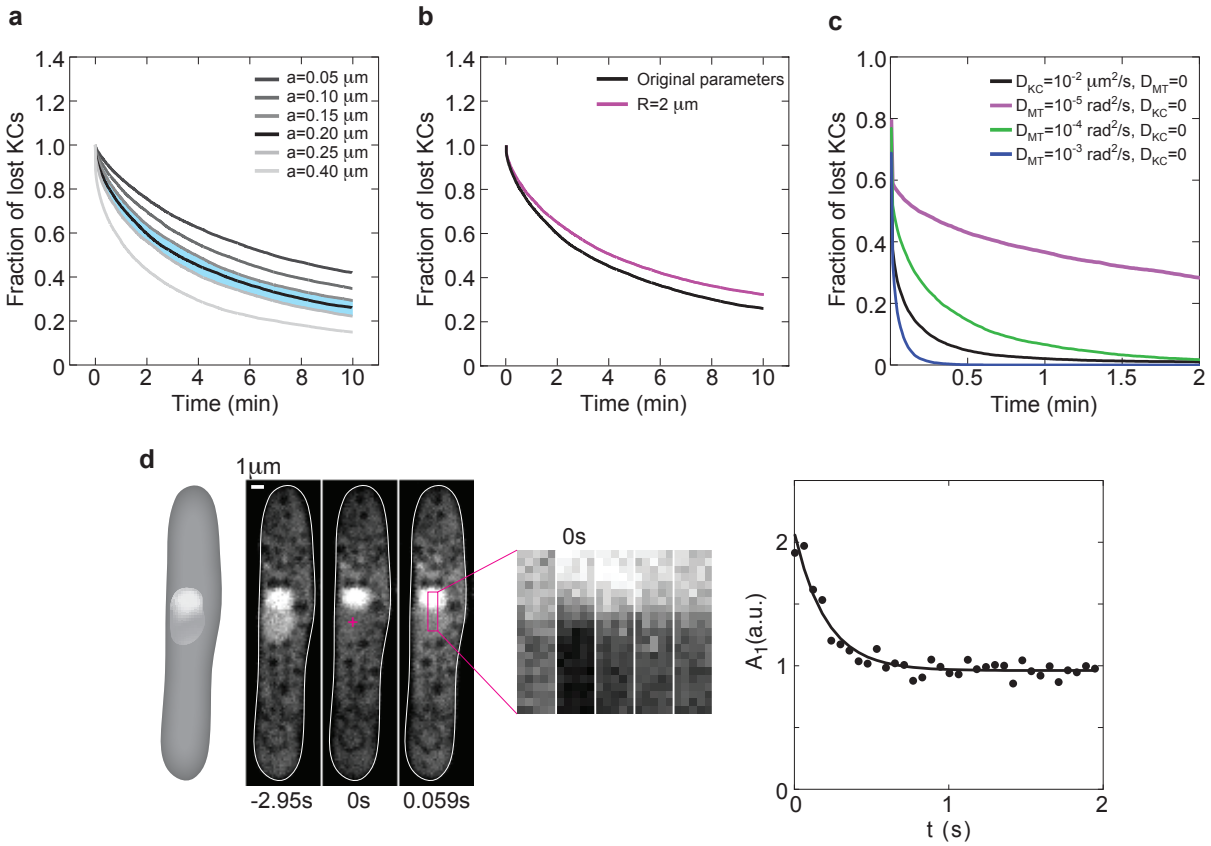

Figure S5 The effect of parameter changes in the model on the capture process and the measurement of the diffusion coefficient of GFP in the nucleus. (**a**) The effect of KC size, a, on the capture process. The curve for a = 0.2 μm is redrawn from Fig. 3c, while the other curves correspond to different KC sizes (see legend). All other parameters are as in Fig. 3c. The blue area between a = 0.15 and a = 0.25 corresponds to the experimental uncertainty in the estimation of a. (**b**) The effect of the nuclear size, R, on the capture process. Curves are shown for R = 1.5 μm (original parameters, redrawn from Fig. 3c) and for R = 2 μm, with other parameters as in Fig. 3c. The latter value was chosen to match the volume of an elongated nucleus, with the short axis of 3 μm and the long axis of 6 μm, as measured in our experiments (Table 1). The elongated geometry of the nucleus consists roughly of two hemi-spherical caps with a radius of 1.5 μm and a cylinder of the same radius. Therefore, we chose to approximate this geometry with a sphere of R = 1.5 μm. (**c**) Results from the model with parameters that are relevant for higher eukaryotic cells. We compare the case where only the KC diffuses (black curve, D_{MT} = 0) and the case where only the MT diffuses, for 3 different values of D_{MT} (see legend). The value D_{MT} = 10^{-5} rad^2/s corresponds to thermally driven angular diffusion of a cylinder of length L = 8 μm and diameter d = 0.025 μm in a medium of viscosity η = 2600 cP (this is the viscosity of the *S. pombe* nucleoplasm, see Fig. S3b). We expect the value D_{MT} = 10^{-4} rad^2/s to be more relevant for higher eukaryotic cells because the viscosity of higher eukaryotic cells is roughly 10 times smaller than the viscosity of the *S. pombe* nucleoplasm (see Supplementary Note 1). The remaining parameters are based on Ref.[11]: n = 250, L = 8 μm, D_{KC} = 0.01 μm^2/s, r_{KC} (t=0) = 7 μm, q_{KC} (t=0) = 10^{-3} rad, a = 0.88 μm, R = 7 μm. We chose r_{KC} and q_{KC} at time 0 such that the KC can be captured by a MT of L = 8 μm. Note that D_{KC} in human cells is 17 times larger than in *S. pombe* (Ref.[11] and this study, respectively). (**d**) FRAP experiments on GFP in the nucleus. From left to right: A scheme and 3 images of a cell expressing NLS-GFP (strain PD31, Supplementary Table S1): before photobleaching, just after photobleaching, and the subsequent image. The cross marks the center of the bleached region (see Methods). A region of interest (ROI, magenta rectangle) with a width of 5 pixels and a length roughly equal to the length of the elongated (mitotic) nucleus, L, was drawn along the nucleus. Next to the images of the cell, a time-lapse sequence of the enlarged ROI in consecutive images shows the recovery of the GFP. The intensities inside the ROI on each image of the movie were summed along the short axis of the ROI. The resulting one-dimensional fluorescence intensity profiles, corresponding to consecutive time points, were used to calculate the temporal decay of the first Fourier mode, which is plotted in the graph on the right. The diffusion coefficient D was calculated from the decay rate of the amplitude of the first Fourier mode $A_1(t)$, as described by Elowitz et al[12]. Circles indicate data points, the solid line is a 3-parameter fit to the function $A_1(t) = A_1(0)\exp(-\pi^2 Dt/L^2)$+offset. For this particular example we get a diffusion coefficient D=3.7 μm^2/s. Repeating this process we obtained the diffusion coefficient of GFP in the nucleus, D=5.6±2.8 μm^2/s (mean±s.d., n=12 cells). The diffusion coefficient of GFP in the cytoplasm was D=8.6±2.2 μm^2/s (mean±s.d., n=8 cells; the strain is described in Methods).

Supplementary Movie Legends

Movie S1 Capture of a lost kinetochore by the tip of a polar microtubule (end-on attachment). Live cell microscopy of an *S. pombe* mitotic cell, expressing tubulin labeled with GFP (green), and the kinetochore protein Ndc80p labeled with tdTomato (magenta); strain AH01 (Table S1). Images were acquired at 2 s intervals. The video is displayed at 15 fps. Time of recovery after cold stress is indicated in minutes:seconds. Scale bar represents 1 µm. The movie corresponds to Fig. 1c.

Movie S2 Capture of a lost kinetochore by the lateral side of a polar microtubule (lateral attachment). Live cell microscopy of an *S. pombe* mitotic cell, expressing tubulin labeled with GFP (green), and the kinetochore protein Ndc80p labeled with tdTomato (magenta); strain AH01 (Table S1). Images were acquired at 2 s intervals. The video is displayed at 15 fps. Time of recovery after cold treatment is indicated in minutes:seconds. Scale bar represents 1 µm. The movie corresponds to Fig. 1d.

Movie S3 Pivoting of polar microtubules around the SPB in a cell expressing Mal3-GFP. Live cell microscopy of an *S. pombe* mitotic cell, expressing Mal3-GFP and Sid4 (SPB marker) labeled with GFP; strain YC001 (Table S1). Note that Mal3-GFP visualizes the movement of the microtubule tip, which allows us to observe the pivoting of a growing microtubule. Mal3p is not present at the end of shrinking microtubules. Images were acquired at 250 ms intervals. The green line marks the position used to make the kymograph shown in Supplementary Fig. S3a. The video is displayed at 15 fps. Time is indicated in seconds. Scale bar represents 1 µm.

Movie S4 Pivoting of polar microtubules in a cell treated with AMP-PNP. Live cell microscopy of an *S. pombe* mitotic cell treated with 50 mM AMP-PNP (strain KI061, Table S1). Images were acquired at 2.2 s intervals. The video is displayed at 15 fps. Time from the beginning of AMP-PNP treatment is indicated in minutes:seconds. Scale bar represents 1 µm. The movie corresponds to Fig. 2a.